# SYNTHETIC JET ACTUATION FOR BOUNDARY LAYER RE-ENERGIZATION AND PHYSIO-CYBER SIMULATIONS

#### J. D. B. Wylie

Dept. Mech., Aero., & Nucl. Eng. Rensselaer Polytechnic Institute Troy, NY 12180 wyliej@rpi.edu

# **S. Suryanarayanan** Dept. Mech. Eng.

The University of Akron Akron, OH 44325 ssuryanarayanan@uakron.edu

#### A. Jariwala

Dept. Aero. Eng. The University of Texas at Austin Austin, TX 78712 akshit@utexas.edu

## E. Bakolas

Dept. Aero. Eng.
The University of Texas at Austin
Austin, TX 78712
bakolas@austin.utexas.edu

# M. Amitay

Dept. Mech., Aero., & Nucl. Eng. Rensselaer Polytechnic Institute Troy, NY 12180 amitam@rpi.edu

#### A. Burtsev

Dept. Aero. Eng.
The University of Texas at Austin
Austin, TX 78712
anton.burtsev@austin.utexas.edu

#### D. Goldstein

Dept. Aero. Eng.
The University of Texas at Austin
Austin, TX 78712
david@oden.utexas.edu

#### INTRODUCTION

Separated flows exist in several relevant external flow scenarios: wind turbine blades, stalled airfoils, compressor blades, etc. The control of these flows leads to improved performance characteristics, increased lift-to-drag ratios, and enhanced fuel efficiency. Typical active methods for separation control include steady blowing or suction, synthetic jets (SJs), sweeping jets, and plasma actuators to name a few (Cattafesta & Sheplak, 2011). These control strategies are effective but often come at the cost of high energy or mass expenditures, and as a result, the flow control is less airworthy since it requires large support systems. This work details an investigation of an improved method for separation control where the control exclusively targets regions of high turbulent kinetic energy (TKE) and momentum surplus. Synthetic large scale motions (LSMs) are generated as a proxy for naturally occurring turbulent boundary layer (TBL) LSMs, sources of high TKE, to re-energize the boundary layer.

In TBLs, LSMs are often identified by low- or high-speed streaks near the wall or the rounded, billowing patterns near the boundary layer edge (Kim & Adrian) [1999]. Lee & Sung, 2011). These LSMs are thought to contain several hairpin vortices, which consist of a head and two near-parallel legs angled at roughly 45° to the surface (Zhou et al.), [1999]. Adrian et al., 2000). The existence of these structures was first identified by two-point hot wire correlations and later seen in flow visualization and particle image velocimetry (PIV) experiments.

The flow field resulting from issuing a rectangular, finite-span synthetic jet into a laminar crossflow has been shown to generate vortex ring/hairpin vortex patterns in a repeatable fashion (e.g., Van Buren *et al.*, 2016). Other works have shown the effects of combining a transverse rectangular synthetic jet at different pitch angles and a turbulent crossflow (e.g., Housley 2020; Straccia & Farnsworth 2022). As such, a rectangular synthetic jet is used in the present work for generating repeatable hairpin trains in both laminar and turbulent bound-

ary layers to simulate naturally-occurring turbulent LSMs.

This work uses a jet-assisted surface-mounted actuator (JASMA) to entrain the artificial hairpin vortices downward. This actuator adds a synthetic jet orifice to the downstream side of a finite aspect ratio circular cylinder, or pin. It has been shown that downwash from the hybrid JASMA can exceed that of the passive pin (Gildersleeve) [2018].

Preliminary computational efforts have been made to generate and control synthetic hairpin trains (Jariwala *et al.*), 2022) and identify and control naturally occurring LSMs (Tsolovikos *et al.*), 2021) for separation bubble control (Tsolovikos *et al.*), 2023). Experimental work has also been conducted to generate and control synthetic LSMs using synthetic jets in a laminar boundary layer (Wylie & Amitay), 2024). Controlled LSMs resulted in increased localized downwash, TKE, and streamwise momentum.

For the sake of accelerating exploratory research, it is of particular interest to find methods of assimilating experimental data from a limited spatial domain into numerical simulations. Several instances of pairing between experiments and simulations have been shown in literature. Methods include adjoint and variational data assimilation techniques (Gronskis et al., 2013), a modified-Spalart method (Lund et al., 1998), nearest neighbor and radial basis function methods (Appelbaum et al.) 2021), and linear stochastic estimation (LSE) (Druault et al.) 2004). Previous efforts by the authors have shown that experimental data from a laminar boundary layer (LBL) could be successfully assimilated (Jariwala et al., 2024). To pair the experiments with simulations more closely, this work utilizes a streamwise-normal experimental data plane to act as a DNS inflow boundary condition (BC) for a hairpin generation case. The experimental data are bi-linearly interpolated to match the DNS grid size and linearly interpolated in time to match the time-stepping required.

This work explores the role of synthetic jet actuation in both the novel boundary layer re-energization technique and in developing physio-cyber simulations for accelerating research on this topic. The latter portion explores a novel flow reconstruction technique for integrating experimental data with the purpose of filling in the gaps in experimental measurements (e.g., wall shear stress) and replicating experiments.

#### **SETUP**

Two sets of experiments were conducted at Rensselaer Polytechnic Institute (RPI). The first set was conducted in a flat plate laminar boundary layer for generating the inflow BC for a physio-cyber simulation, which are described in more detail in this section. The second set of experiments in a zero pressure gradient flat plate TBL used a synthetic jet actuator to generate synthetic hairpin vortices. These turbulent LSMs were controlled to investigate boundary layer re-energization and ultimately separation control.

#### **Laminar Boundary Layer Experiments**

An LBL was generated on the floor of the small-scale wind tunnel at RPI at a free stream velocity of 10 m/s. This was validated against the Blasius solution with good agreement. A wall-mounted synthetic jet orifice (12 mm  $\times$  1 mm), pitched downstream at an angle of  $\alpha_{sj}=45^{\circ}$  to the tunnel floor, was run at a driving frequency of 1.1 kHz. A blowing ratio of  $C_{b_{sj}}=V_{peak}/(\pi U_{\infty})=0.5$  was used where  $V_{peak}$  is the peak SJ velocity at the orifice plane and  $U_{\infty}$  is the free stream velocity. The LBL experimental setup can be seen in Figure [1]

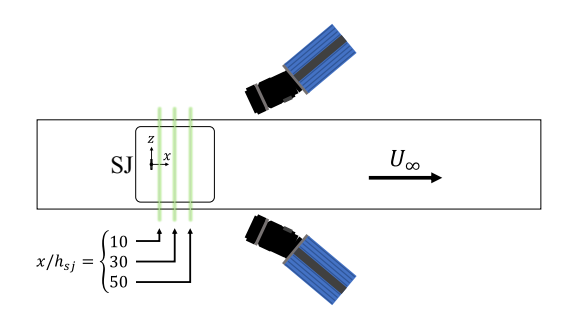


Figure 1: Schematic of the cameras and laser sheet configuration for the stereoscopic LBL experiments.

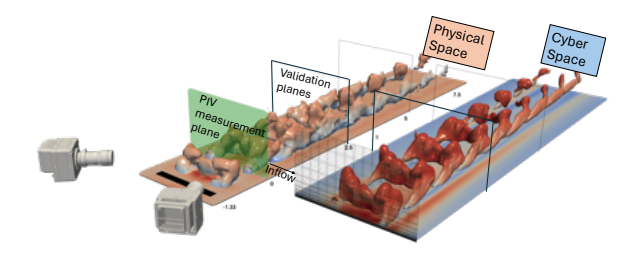


Figure 2: Schematic representation of the hybrid physiocyber approach. Reproduced from Jariwala *et al.* (2023).

Stereoscopic PIV (SPIV) image pairs were acquired in the streamwise-normal orientation at three planes in the domain downstream of the SJ using the DaVis 8.4 software from LaVision GmbH. 250 image pairs were acquired with two 2 MPx

CCD cameras at 72 equally-spaced phases of the synthetic jet actuation cycle. The disparity vector between camera focal and laser planes was corrected at each spanwise-normal plane using an SPIV self-calibration algorithm. Vectors were then processed using an SPIV cross-correlation algorithm with an initial pass of 48 pixel  $\times$  48 pixel windows followed by two passes of 24 pixel  $\times$  24 pixel windows, each with 50% overlap. The instantaneous vector fields were smoothed using a 3  $\times$  3 filter. The resulting vector fields had a resolution of 2.97 vectors/mm.

### **Turbulent Boundary Layer Experiments**

Additional experiments were conducted to explore the effect of weak JASMA control to entrain synthetic hairpin trains in a TBL. A TBL was achieved by tripping the flow over a flat plate model in the large-scale wind tunnel at RPI. A zero pressure gradient was achieved over the model using an elliptic leading edge and an adjustable trailing edge flap. The nominal boundary layer profile was compared favorably against the log-law profile for  $y^+ \gtrsim 30$ . Separate SJ and JASMA modules were positioned towards the end of the plate for generation and later control of artificial LSMs. The pitched synthetic jet  $(\alpha_{si} = 45^{\circ})$  was actuated at a driving frequency of 1.8 kHz. A finite-span cantilevered pin with a height of  $h_p/\delta = 0.28$ was placed downstream of the synthetic jet. A synthetic jet orifice (6 mm  $\times$  0.5 mm) was placed on the downstream side of the pin. The resulting JASMA was actuated at the same 1.8 kHz frequency as the synthetic jet. Schematics of the flat plate model and actuator modules are shown in Figures 3a and 3b respectively. A depiction of the phase difference between the SJ and JASMA is shown in Figure 3c

Planar PIV image pairs were acquired in the spanwisenormal orientation along the centerline in the domain upstream and downstream of the JASMA. 1000 pairs were acquired with a LaVision 2 MPx Imager LX CCD camera for the timeaveraged and phase-locked (to the synthetic jet) data to allow for convergence of the time-averaged and phase-averaged velocity and RMS values. The camera was outfitted with a 100 mm lens. The image pairs were processed with a crosscorrelation algorithm in the DaVis 8.4 software using interrogation windows in two consecutive passes. The first pass consisted of 32 × 32 pixel windows with 50% overlap followed by two passes of 16 × 16 pixel windows with 50% overlap. Images were initially masked to remove laser reflection and treated with a time filter subtraction to remove the average noise from the images. The resultant vector fields were post-processed with a 3 × 3 smoothing kernel before being averaged into single average velocity fields with a resolution of 1.96 vectors/mm.

## **Numerical Setup**

A high-fidelity DNS solver at the University of Texas at Austin was used to conduct a physio-cyber simulation to corroborate test cases of SJ actuation in the LBL crossflow. Additionally, this methodology was extended towards reconstructing a TBL. The nek5000 high-order spectral element solver (Fischer et al.) [2007) was used to solve the governing incompressible, nondimensional Navier Stokes equations. The mesh contains a rectangular domain comprising a portion of the experimental domain. The computational domain is split into spectral elements with 100, 15, and 24 in the streamwise, vertical, and spanwise directions, respectively. Each spectral element represents the flow field in the form of a 7th-order Gauss-Lobatto-Legendre polynomial.

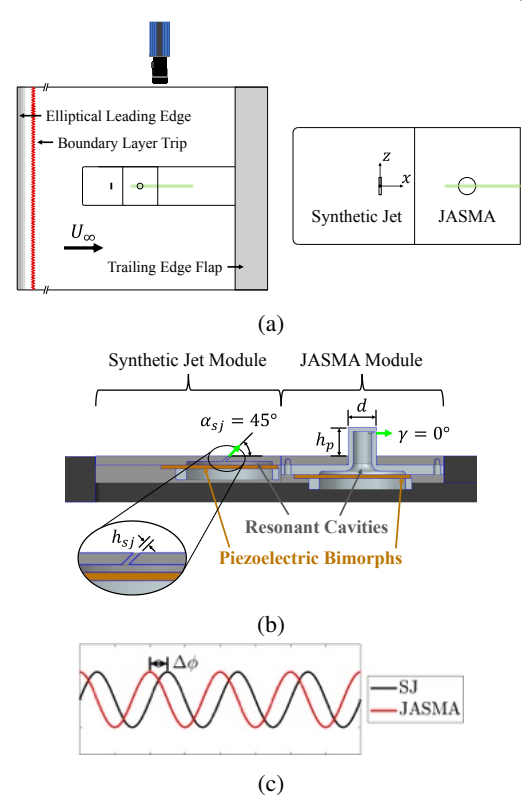


Figure 3: Schematics of the camera and laser sheet configuration for the planar PIV TBL experiments (a), section views of the actuator modules for the TBL experiments (b), and a schematic with the relative phase shift between actuator input signals (c).

The BCs consisted of a no-slip condition at the floor, periodic BCs at the spanwise limits, and outflow BCs at the top and outlet (expressed as  $[-p+v(\nabla U)\cdot n=0]$ ) where n is the unit normal vector. For the upstream BC in the LBL case, planar SPIV data in the streamwise-normal orientation from experimental setup were interpolated and pre-processed to fit the computational domain. The data were bilinearly interpolated in space and linearly interpolated in time to match the much finer DNS grid and temporal resolutions. In contrast, for the TBL, temporal and spatially resolved wind tunnel data were not utilized. Instead, a precursor test case was conducted using TBL data obtained from a separate DNS with a momentum thickness Reynolds number,  $Re_{\theta}$ , comparable to that of the TBL experiments. From this precursor simulation, a plane of data was extracted as could be done from a real experiment.

#### **RESULTS**

This section presents numerical results derived from DNS simulations, employing experimental or numerical data as an inflow BC. The physio-cyber tests were initially conducted in an LBL setting to demonstrate feasibility before considering a TBL scenario. Furthermore, representative results from the TBL experiments are included in this section, illustrating the efficacy of the control concept and potential applications for future separation control.

#### **Physio-Cyber DNS for Hairpin Generation**

Physio-cyber simulations utilize time-varying unsteady spatially discrete velocity data obtained from experiments as

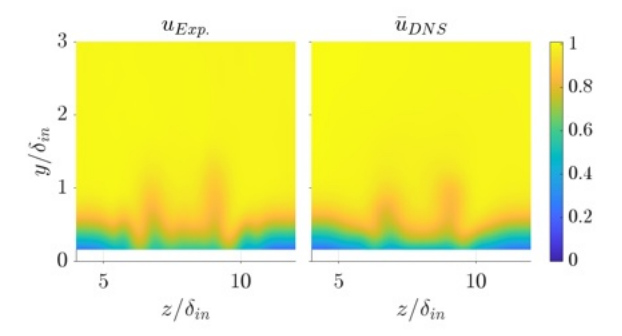


Figure 4: Comparison of instantaneous normalized streamwise velocity  $(u/U_{\infty})$ : raw PIV on the left and filtered DNS on the right.

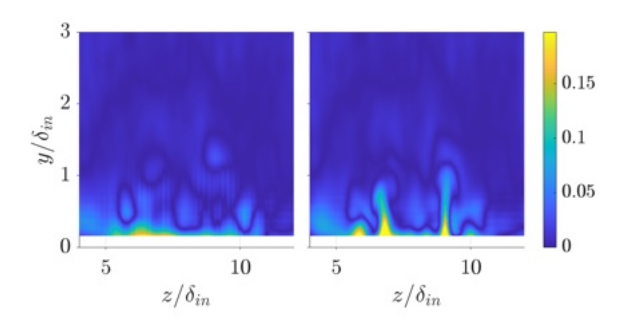


Figure 5: Absolute error ( $|u_{\rm Exp.} - \overline{u}_{\rm DNS}|$ ) in normalised streamwise velocity with (left) and without (right) Gaussian smoothing.

an inflow BC for DNS. Preliminary results for this approach have previously been demonstrated (Jariwala et al.) 2024). A schematic concept is illustrated in Figure 2 showing sequence of hairpins produced from data collected through LBL experiments. Further details regarding the divergence correction scheme to remove PIV stochastic noise in the velocity field and an interpolation scheme to map the velocity data onto a DNS grid can be found in that paper. A strong qualitative agreement was observed between the volumetric SPIV dataset and the flow reconstructed through its simulated counterpart with a hybrid data assimilation at the DNS inflow region. To extend this work, the DNS data was filtered using a spatial lowpass filter. In order to establish an analogy between the reconstructed flow-field and an SPIV field, which inherently suffers from limitations in spatial resolution, a smoothing operation becomes necessary. A simple Gaussian-type filter kernel was selected with a kernel width (smoothness factor) of 0.4.

A snapshot of the filtered DNS result is shown in Figure 4. where  $\bar{u}$  represents a mild streamwise volume averaging of the DNS data to accommodate the finite thickness of the laser sheet in the PIV setup. Figure 5 compares changes in absolute error  $|u_{\rm Exp.} - \bar{u}_{\rm DNS}|$  between filtered and unfiltered DNS data. It is evident that Gaussian blurring has brought the DNS data closer to the PIV (Figure 5). Comparison was performed at the plane  $x/h_{sj} = 50$  (see Figure 1) while using  $x/h_{sj} = 30$  plane downstream of the SJ as inflow data to the DNS.

#### **Turbulent Boundary Layer Flow Reconstruction**

Building upon the promising results from the the physiocyber simulation mentioned in the previous section, similar tests were conducted in a TBL setting, showcasing its applicability to TBL flow field reconstruction.

The data were collected on a uniform rectilinear grid with spatial and temporal resolutions akin to the TBL experiments. Specifically, the spacing in the spanwise ( $\Delta z$ ) and wall-normal ( $\Delta y$ ) directions was  $0.05\delta_{in}$ , while the temporal acquisition frequency was  $0.05\delta_{in}/U_{\infty}$ . The sampling grid, which was significantly coarser than the DNS grid, resulted in a non-zero divergence error in the sampled data. Similar to the physic-cyber simulation for the LBL case, equivalent pre-processing steps were undertaken to prepare the data suitable to use as an inflow BC.

A contour plot of instantaneous streamwise velocity is shown in Figure [6] comparing reconstructed field (6p) with the original DNS (6a) from which data were sampled. A closer examination reveals prominent large-scale similarities in the outer region of the TBL while the match is poorer in the viscous sub-layer. These disparities along the streamwise direction are evident in Figure [7] showing the absolute difference in instantaneous streamwise velocity between the original reference DNS and the reconstructed flow field. The mismatch in the outer region and sub-layer becomes particularly prominent beyond  $x/\delta_{in} > 20$ , indicating the onset of non-linear effects.

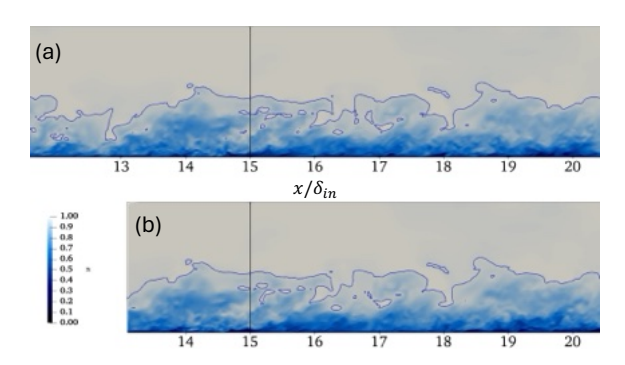


Figure 6: Comparison of instantaneous streamwise velocity: Reference DNS (a), Reconstructed flow field through inflow BC derived from planar experimental data collected at  $x/\delta_{in}=13$  (b). Contour line corresponding to  $0.99U_{\infty}$  is shown in dark blue highlighting viscous superlayer. The vertical lines at  $x/\delta_{in}=15$  indicate the profile location in Figure [8].

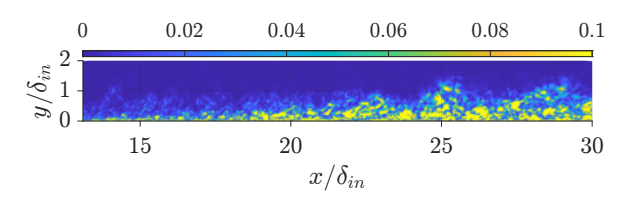


Figure 7: Absolute error in normalised instantaneous streamwise velocity between original reference DNS and reconstructed field.

In general, acquired PIV data is noisy and somewhat blurry, due to smoothing and the overlap of interrogation windows. Additionally, due to laser reflection, data closer to the wall is often missing. To assess the quality of the reconstructed field and replicate these PIV deficits, different pre-processing steps were examined: 1) Gaussian noise was added with zero mean and a variance of  $1\%U_{\infty}$ ; 2) A divergence correction scheme was employed; 3) A Gaussian-like smoothing kernel was used to blur the data; 4) Lastly, a few points closer to the

wall were not recorded in the sampling grid to account for laser flare limitations.

Figure 8 illustrates variations in the  $u^+ = u/u_\tau$  profile across the TBL at  $x/\delta_{in} = 15$  (indicated by the vertical black lines in Figure 6). A total of five different cases were compared against the reference DNS case (dark blue curve): sampled data without any pre-processing (Raw - red curve), divergence-corrected data (Div. Corr - yellow curve), divergence-corrected data with a few points missing close to the wall (PIV Div. Corr. - purple curve), sampled data with Gaussian blurring (PIV smooth - green curve), and sampled data with added noise (PIV noise - light blue curve).

The viscous sub-layer region  $(y^+ < 5)$  demonstrates agreement among all the different cases as expected since the profiles are scaled by their respective inner variables. The most noticeable differences emerge in the log-layer  $(20 < y^+ < 180)$ , as depicted in Figure 8 However, the mean statistics profiles  $(u^+ \text{ vs. } y^+)$  collapse further downstream, as all cases are run with the same Reynolds number, following the law of the wall.

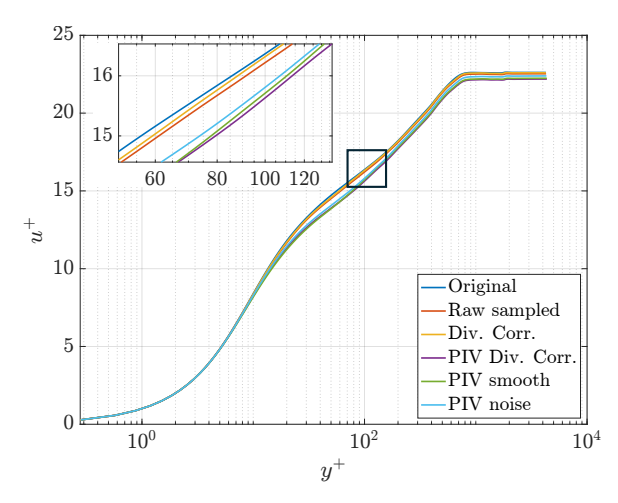


Figure 8:  $u^+ = u/u_\tau$  versus  $y^+ = yu_\tau/v$  at  $x/\delta_{in} = 15$  for different scenarios: Original - reference DNS, Raw - sampled data directly used as inflow without any preprocessing as in Figure 6b, Div. Corr - sampled data contaminated with white noise with divergence correction scheme, PIV Div. Corr. - Divergence corrected data with a few points missing close to the wall, PIV smooth - sampled data with Gaussian smoothing, PIV noise - sampled data with added noise.

# Controlling Turbulent Boundary Layer Hairpin Trains using Synthetic Jets

A parameter study was conducted to determine control parameters for the JASMA. The JASMA height  $(h_p)$ , pitch angle  $(\gamma)$ , blowing ratio  $(C_{b_J})$ , and phase relative to the synthetic jet used for LSM generation  $(\Delta\phi)$  were varied. For brevity, a few representative cases are presented.

The generation of artificial hairpin trains is compared with the JASMA actuation and combined SJ+JASMA interactions in Figure  $\boxed{0}$  Color contours of phase-locked wall-normal velocity with the time-averaged values subtracted  $((V_\phi-\overline{V})/U_\infty)$  are displayed with corresponding vectors overlaid.  $V_\phi$  is the phase-averaged vertical velocity component, and  $\overline{V}$  is the time-

averaged vertical velocity component. The alternating trains of up and down relative motion are indicative of hairpin vortex trains where the individual hairpin heads are comprised of one pair of upwash and downwash regions (red and blue, respectively). The SJ-only case (Figure 9a) shows an upward trajectory of the artificial hairpin vortices as they gradually diffuse but remain coherent in terms of  $(V_{\phi} - \overline{V})/U_{\infty}$  contours. Actuating only the JASMA yields a hairpin train with a slower convective velocity than that of the SJ vortices as evidenced by the smaller spacing in Figure 9b. The JASMA vortices are entirely diffused by x/d = 9. Figures 9c and 9d depict the results from applying the JASMA actuation to the SJ hairpin train for two particular phase differences between the SJ and JASMA (i.e.,  $\Delta \phi = 90,270^{\circ}$ , respectively). As seen by the difference in  $(V_{\phi} - \overline{V})/U_{\infty}$  contours, the relative phase greatly affected the interactions of the vortices. At  $\Delta \phi = 90^{\circ}$  a constructive interaction yields an increased vortex strength (Figure 9)c, while at  $\Delta \phi = 270^{\circ}$  the vertical velocity oscillations are greatly weakened (Figure 9d). Overall, actuating the JASMA and the SJ together leads to a downward change in the trajectory of the SJ vortices, suggesting that the control JASMA has redirected the synthetic hairpin train.

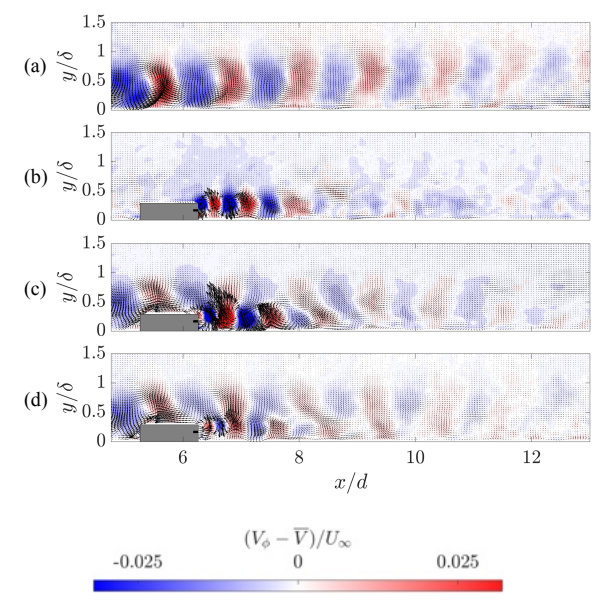


Figure 9: Color contours of phase-locked vertical velocity with the time-averaged values subtracted and time-average-subtracted velocity vectors overlaid at a common phase ( $\theta=0^{\circ}$ ) for the cases: SJ-only (a), JASMA-only (b), SJ+JASMA with  $\Delta\phi=90^{\circ}$  (c), and SJ+JASMA with  $\Delta\phi=270^{\circ}$  (d). The synthetic jet was operated with a blowing ratio of  $C_{b_{sj}}=0.54$ . The JASMA had a height of  $h_p/\delta=0.28$  with ( $\gamma=0^{\circ}$ ) and a blowing ratio of  $C_{b_J}=0.32$ . The mean flow direction is from left to right.

Next, a comparison of the time-averaged boundary layer profiles at four relative phase differences is shown in Figure 10 at the end of the pin recirculation region (x/d=7.14) and farther downstream (x/d=12.76). At both locations, the phase differences of  $\Delta \phi = 90^{\circ}$  and  $270^{\circ}$  show the most and least streamwise momentum addition to the near wall region, respectively. This is consistent with the strength of the velocity oscillations seen in Figure 9 suggesting that stronger vortex

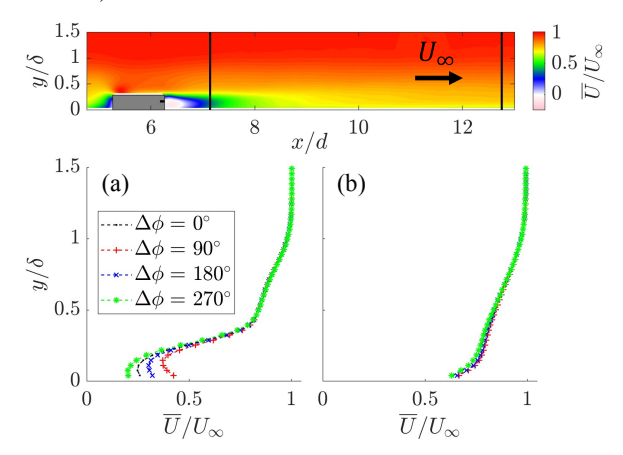


Figure 10: Time-averaged, normalized, streamwise velocity profiles at x/d=7.14 (a) and 12.76 (b) comparing phase differences between the SJ and JASMA of  $\Delta\phi=0.90,180$ , and 270°. The SJ was operated with a blowing ratio of  $C_{b_{sj}}=0.54$ . The JASMA had a height of  $h_p/\delta=0.28$  and was unpitched ( $\gamma=0^\circ$ ) with a blowing ratio of  $C_{b_J}=0.32$ . Representative color contour schematics with the profile locations indicated by the black lines are shown above.

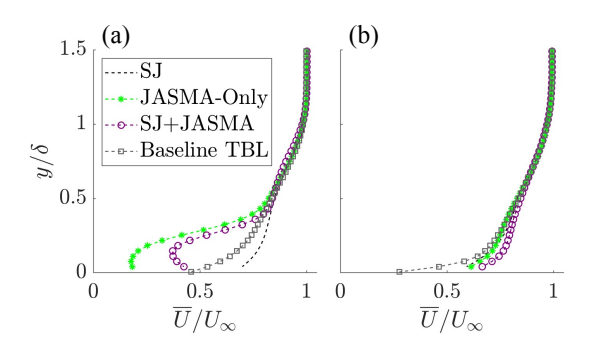


Figure 11: Time-averaged, normalized, streamwise velocity profiles at x/d=7.14 (a) and 12.76 (b) comparing various control cases. The SJ was operated with a blowing ratio of  $C_{b_{sj}}=0.54$ . The JASMA had a height of  $h_p/\delta=0.28$  and was unpitched ( $\gamma=0^\circ$ ) with a blowing ratio of  $C_{b_J}=0.32$  and  $\Delta\phi=90^\circ$ .

interactions lead to greater mixing and increased streamwise momentum.

Finally, the time-averaged streamwise velocity profiles are plotted in Figure [1] to compare the actuation cases at the same two streamwise locations from Figure [10]. All cases with a static pin or JASMA introduce a wake deficit clearly seen at x/d=7.14. The SJ+JASMA case shows the highest momentum at both locations of the cases with active control. In fact, at the farther downstream location higher streamwise momentum is seen for the control case compared to either the SJ-only or TBL baseline cases. These results suggest that the SJ+JASMA case is effective at introducing streamwise momentum downstream of the control.

#### DISCUSSION

The results examine the effect of a JASMA for control of artificial hairpin vortices, representative of LSMs in a TBL.

Control at a relatively low blowing ratio succeeded in amplifying the effects of the synthetic LSMs created by the SJ. Proper timing control affected a beneficial effect in streamwise momentum addition and vortex amplification. The streamwise velocity profiles and vertical velocity color contours suggest that the most effective phasing between the actuators was tied to amplification of the artificial LSM vortices and reduction of the recirculation region behind the JASMA. When actuated together, the SJ and JASMA yielded higher streamwise momentum downstream than the SJ-only case and the unaltered TBL baseline, indicating that this control strategy has potential for separation control. The contributions of these actuators do not seem to linearly superpose, suggesting also that the interaction nonlinearly achieves TBL re-energization. For example, very close to the wall, the SJ+JASMA case has higher momentum than what would be result from the simple addition of the two effects. This suggests that the JASMA steers synthetic hairpins towards the wall, enhancing momentum transport. Though further analysis is required, this supports control solutions provided previously (Tsolovikos et al., 2021; Tsolovikos, 2023). Future experimental work will explore a larger region of the flow downstream of the JASMA as well as the effect of different LSM.

The present physio-cyber simulation demonstrates encouraging results in reconstructing downstream flow fields, utilizing necessarily restricted time-varying inflow BCs derived from planar three-component velocity measurements corresponding to realistic SPIV measurements. This study addresses stochastic noise in the data, such as PIV noise, and missing data close to the wall on a relatively coarser grid over only portion of the wind tunnel at crude time resolution, considering their overall effect on the reconstructed flow. Figure 8 highlights discrepancies in mean flow statistics, particularly in the log-layer when data near the wall is missing. Further analysis downstream of the inflow plane  $(x/\delta_{in} > 15)$  reveals significant improvement in the mean flow profile ( $u^+$  vs.  $y^+$ ), attributed to inner wall variable scaling and the law of the wall. Figure 7 highlights larger discrepancies when comparing instantaneous streamwise velocity beyond  $x/\delta_{in} > 20$  due to onset of non-linear effects. Further examination will be carried out to quantify these differences in terms of energy spectra, Reynolds stresses, and two-point correlation coefficient. Future DNS runs will integrate TBL inflow data obtained from actual SPIV measurements, facilitating the derivation of statistical flow quantities that may not be easily measurable in the experimental setup otherwise.

#### **REFERENCES**

- Adrian, R.J., Meinhart, C.D. & Tomkins, C.D. 2000 Vortex organization in the outer region of the turbulent boundary layer. *Journal of Fluid Mechanics* 422, 1–54.
- Appelbaum, J., Ohno, D., Rist, U. & Wenzel, C. 2021 DNS of a turbulent boundary layer using inflow conditions derived from 4d-ptv data. *Experiments in Fluids* 62.
- Cattafesta, L.N. & Sheplak, M. 2011 Actuators for active flow control. *Annual Review of Fluid Mechanics* **43**, 247–272.
- Druault, P., Lardeau, S., Bonnet, J.-P., Coiffet, F., Delville, J., Lamballais, E., Largeau, J.-F. & Perret, L. 2004 Generation of three-dimensional turbulent inlet conditions for large-eddy simulation. *AIAA J.* **42** (3), 447–456.

- Fischer, P., Lottes, J. & Tufo, H. 2007 Nek5000.
- Gildersleeve, S.M. 2018 Fundamental investigation of the flow around a finite span low aspect ratio pin and its application to flow control. PhD thesis, Rensselaer Polytechnic Institute
- Gronskis, A., Heitz, D. & Mémin, E. 2013 Inflow and initial conditions for direct numerical simulation based on adjoint data assimilation. *Journal of Computational Physics* 242, 480–497.
- Housley, K.W. 2020 Synthetic jet actuator fabrication: Modeling, quantification, and implementation. PhD thesis, Rensselaer Polytechnic Institute.
- Jariwala, A., Tsolovikos, A., Suryanarayanan, S., Bakolas, E. & Goldstein, D. 2022 On the effect of manipulating large scale motions in a boundary layer. In AIAA AVIATION Forum, pp. 1–12. American Institute of Aeronautics and Astronautics.
- Jariwala, A., Wylie, J., Amitay, M. & Goldstein, D. 2023 Generation of hairpin vortices via physio-cyber data assimilation approach. In *Gallery of the Fluid Motion of the American Physical Society*. APS.
- Jariwala, A., Wylie, J.D.B., Tsolovikos, A., Suryanarayanan, S., Bakolas, E., Amitay, M. & Goldstein, D.B. 2024 Generation of hairpin vortices using a hybrid physio-cyber data assimilation approach. In AIAA SCITECH 2024 Forum, p. 0931. American Institute of Aeronautics and Astronautics.
- Kim, K.C. & Adrian, R.J. 1999 Very large-scale motion in the outer layer. *Physics of Fluids* **11**, 1–6.
- Lee, J.H. & Sung, H.J. 2011 Very-large-scale motions in a turbulent boundary layer. *Journal of Fluid Mechanics* **673**, 80–120.
- Lund, T.S., Wu, X. & Squires, K.D. 1998 Generation of turbulent inflow data for spatially-developing boundary layer simulations. *Journal of Computational Physics* 140, 233– 258.
- Straccia, J.C. & Farnsworth, J.A.N. 2022 On the vortex dynamics of synthetic jet-turbulent boundary layer interactions. *arXiv:2205.07370*.
- Tsolovikos, A. 2023 Data-driven modeling and control of high-dimensional and nonlinear systems with application to turbulent flows committee. PhD thesis, The University of Texas at Austin.
- Tsolovikos, Alexandros, Jariwala, Akshit, Suryanarayanan, Saikishan, Bakolas, Efstathios & Goldstein, David 2023 Separation delay in turbulent boundary layers via model predictive control of large-scale motions. *Physics of Fluids* 35 (11)
- Tsolovikos, A., Suryanarayanan, S., Bakolas, E. & Goldstein, D. 2021 Model predictive control of material volumes with application to vortical structures. AIAA J. 59, 4057–4070.
- Van Buren, T., Leong, C.M., Whalen, E. & Amitay, M. 2016 Impact of orifice orientation on a finite-span synthetic jet interaction with a crossflow. *Physics of Fluids* **28** (3).
- Wylie, J.D.B. & Amitay, M. 2024 Control of artificially-generated hairpin vortices in a laminar boundary layer. In *AIAA SCITECH 2024 Forum*. American Institute of Aeronautics and Astronautics.
- Zhou, J., Adrian, R.J., Balachandar, S. & Kendall, T.M. 1999 Mechanisms for generating coherent packets of hairpin vortices in channel flow. *Journal of Fluid Mechanics* **387**, 353–396.